

**Spin-carrier coupling induced ferromagnetism and giant resistivity peak in  $\text{EuCd}_2\text{P}_2$** 

V. Sunko <sup>1,2,\*</sup>, Y. Sun <sup>1,2,\*</sup>, M. Vranas <sup>3</sup>, C. C. Homes <sup>4</sup>, C. Lee <sup>2</sup>, E. Donoway <sup>1,2</sup>, Z.-C. Wang <sup>5</sup>, S. Balguri <sup>5</sup>,  
M. B. Mahendru <sup>5</sup>, A. Ruiz <sup>3</sup>, B. Gunn <sup>3</sup>, R. Basak <sup>3</sup>, S. Blanco-Canosa <sup>6,7</sup>, E. Schierle <sup>8</sup>, E. Weschke <sup>8</sup>, F. Tafti <sup>5</sup>,  
A. Frano <sup>3</sup> and J. Orenstein <sup>1,2</sup>

<sup>1</sup>Department of Physics, University of California, Berkeley, California 94720, USA

<sup>2</sup>Materials Science Division, Lawrence Berkeley National Laboratory, Berkeley, California 94720, USA

<sup>3</sup>Department of Physics, University of California, San Diego, California 92093, USA

<sup>4</sup>NSLS II, Brookhaven National Laboratory, Upton, New York 11973, USA

<sup>5</sup>Department of Physics, Boston College, Chestnut Hill, Massachusetts 02467, USA

<sup>6</sup>Donostia International Physics Center, DIPC, 20018 Donostia-San Sebastian, Basque Country, Spain

<sup>7</sup>IKERBASQUE, Basque Foundation for Science, 48013 Bilbao, Spain

<sup>8</sup>Helmholtz-Zentrum Berlin für Materialien und Energie, Albert-Einstein-Straße 15, 12489 Berlin, Germany



(Received 9 August 2022; revised 4 November 2022; accepted 17 March 2023; published 4 April 2023)

$\text{EuCd}_2\text{P}_2$  is notable for its unconventional transport: upon cooling the metallic resistivity changes slope and begins to increase, ultimately 100-fold, before returning to its metallic value. Surprisingly, this giant peak occurs at 18 K, well above the Néel temperature ( $T_N$ ) of 11.5 K. Using a suite of sensitive probes of magnetism, including resonant x-ray scattering and magneto-optical polarimetry, we have discovered that ferromagnetic order onsets above  $T_N$  in the temperature range of the resistivity peak. The observation of inverted hysteresis in this regime shows that ferromagnetism is promoted by coupling of localized spins and itinerant carriers. The resulting carrier localization is confirmed by optical conductivity measurements.

DOI: [10.1103/PhysRevB.107.144404](https://doi.org/10.1103/PhysRevB.107.144404)

## I. INTRODUCTION

First glimpses of phase transitions in new materials are often gained through measurement of the temperature-dependent resistivity  $\rho(T)$ . At a magnetic transition  $\rho(T)$  of a metal generically exhibits a change in slope with  $d\rho/dT$  proportional to the heat-capacity anomaly. This behavior is understood within the Fisher-Langer theory in which enhanced quasiparticle scattering appears as a consequence of critical fluctuations [1]. However, some metallic magnets exhibit features in  $\rho(T)$  more pronounced than a mere change in slope. For example, resistivity peaks have been reported recently near the Néel temperature  $T_N$  in a number of antiferromagnetic (AFM) europium compounds with the general formula  $\text{Eu}M_2C_2$  ( $M = \text{In}, \text{Cd}$ ,  $C = \text{Sb}, \text{As}, \text{P}$ ) [2–7]. In these materials magnetism is localized in  $\text{Eu}^{2+}$  layers, which are separated by low-carrier density itinerant  $M_2C_2$  blocks. They are notable because density-functional theory predicts that their low-energy electronic structure and topology are dramatically altered by the nature of the magnetic order [8–15] and that the different magnetic states are close in energy [16] and are, therefore, experimentally accessible [2, 17–19]. This combination offers the exciting prospect of creating electronic states hypersensitive to external stimuli.

The resistivity of  $\text{EuCd}_2\text{P}_2$ , the subject of this paper (see Sec. I of the Supplemental Material (SI) [20] for sample preparation and characterization, stands out as an extreme example of unconventional temperature dependence, quantita-

tively and qualitatively different from other systems exhibiting a resistivity peak [5]. As shown in Fig. 1, the metallic high-temperature resistivity [green in Fig. 1(c)] undergoes a hundredfold increase with decreasing temperature (blue) and, subsequently, returns to metallic values (purple). Both the rise and the fall of the resistance take place well above the Néel temperature of 11.5 K as determined from the heat-capacity measurements. The peak value of  $\rho$ , which is found at 18 K is suppressed by modest magnetic fields, yielding a giant negative magnetoresistance [5].

Here we use a powerful combination of bespoke magneto-optical techniques and x-ray scattering to show that the anomalous resistivity peak does not arise due to antiferromagnetism, but it is a consequence of a previously unreported time-reversal (TR) breaking that takes place above the Néel temperature. Our results indicate that AFM order is preceded by the formation of ferromagnetic clusters driven by the interaction of localized spin and itinerant charge degrees of freedom. The three resistivity regimes depicted in Fig. 1 are traced to temperature-dependent crossovers from independent fluctuating clusters to the onset of ferromagnetic order.

## II. OPTICAL POLARIMETRY: SYMMETRY BREAKING ABOVE $T_N$

We begin by describing our spatially resolved symmetry-sensitive optical measurements in which we measure the change in the angle of linear polarization ( $d\phi$ ) as a function of sample orientation. Since we cannot physically rotate the sample fixed to piezoelectric scanning stages, we access the same information by rotating the incoming light polarization

\*These authors contributed equally to this work.

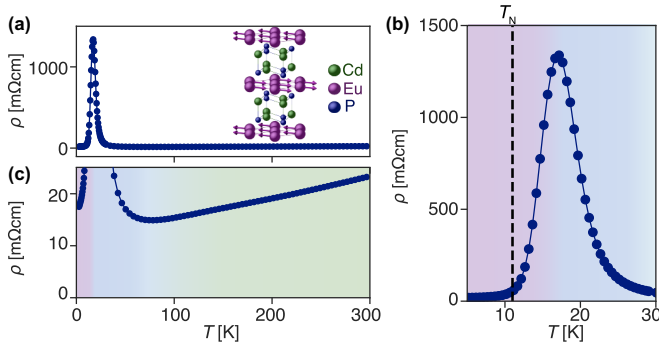


FIG. 1. (a) and (b) The resistivity of  $\text{EuCd}_2\text{P}_2$  (structure in the inset) shows a pronounced peak at 18 K. (c) Above 75 K it exhibits metallic behavior. Data are from Ref. [5].

( $\phi$ ). Once the experimental setup is carefully aligned to preserve the polarization state (SI, Sec. III [20]), the change of polarization upon reflection is given by

$$d\phi \sim A(T) \sin\{2[\phi - \phi_0(T)]\} + B(T), \quad (1)$$

where  $\phi_0(T)$  and  $\phi_0(T) + \pi/2$  indicate the directions of the principal optical axes, and  $A(T)$  and  $B(T)$  are proportional to birefringence and polar magneto-optical Kerr effect (pMOKE). These effects arise from the breaking of rotational symmetry and out-of-plane magnetization  $M_z$ , respectively. To enhance experimental sensitivity, we modulate  $T$  at a frequency  $f \approx 2$  kHz using a second laser beam as a heater, essentially measuring the temperature derivatives of  $A$  and  $B$ ,  $dA$  and  $dB$  [21,22].

This experiment at 2 K reveals a sinusoidal dependence of  $d\phi$  on  $\phi$  [Fig. 2(a), Eq. (1)], corresponding to a nonzero value of  $dA$  and indicating broken rotational symmetry. Figure 2(b) is a map of the spatial distribution of  $\phi_0$ , revealing three birefringent domains with  $120^\circ$  between their principal axes [see Fig. S2(a) of the SI [20] for a histogram of the relative domain populations]. This observation is consistent with spontaneous breaking of  $C_3$  symmetry at the onset of previously reported type-A-AFM order (i.e., alternating ferromagnetic layers with in-plane spins, Ref. [5]) on a triangular lattice.

The first indication of unconventional order in  $\text{EuCd}_2\text{P}_2$  is the observation of nonzero  $dB$ , indicated by the  $\phi$ -independent offset of the sinusoidal curves in Fig. 2(b). As mentioned above, this offset demonstrates the existence of an out-of-plane component of magnetization,  $M_z$ ; we, therefore, refer to it as  $dM_z$  for clarity. The  $dM_z$  map [Fig. 2(c)] shows that domains of  $M_z$  and A-AFM order are highly correlated, suggesting coexistence and strong coupling between the two forms of order. In contrast, reflectivity is uniform across this sample region [see Figs. S1(b)–S1(d)] in the SI [20].

The temperature dependence of  $dA$  shown in Fig. 2(d) exhibits an additional surprising feature: The birefringence that was provisionally attributed to antiferromagnetism does not vanish at  $T_N$ . Rather, with increasing temperature, there is a discontinuous change in slope at  $T_N$  followed by a gradual decrease in amplitude, showing that  $C_3$  symmetry remains broken above  $T_N$ .  $dM_z$  also remains nonzero above  $T_N$  with the polar Kerr signal changing smoothly through the transition. We emphasize that both of these signals indicate static

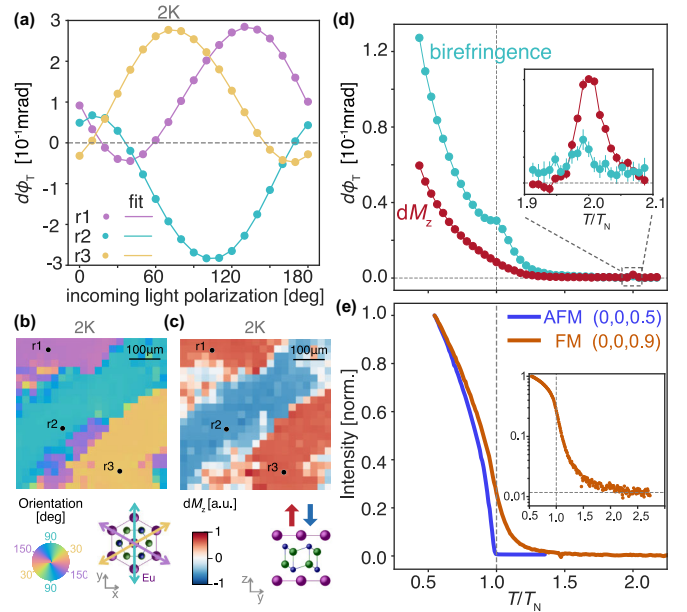


FIG. 2. (a) Thermally modulated polarization rotation as a function of incident polarization and corresponding fits [Eq. (1)], measured at three sample locations (probe: 20  $\mu\text{W}$ , 633 nm; pump: 50  $\mu\text{W}$ , 780 nm, modulated at 2345 Hz). (b) and (c) Maps of (b) principal axis orientation and (c)  $dM_z$ , extracted from the phase and offset of curves, such as those in (a) (step size: 25  $\mu\text{m}$ , light spot diameter: 5  $\mu\text{m}$ ). (d) Thermally modulated birefringence amplitude (teal) and  $dM_z$  (red) as a function of temperature ( $T_N = 11.5$  K). Both signals onset at  $\sim 2T_N$  (the inset). (e) Normalized antiferromagnetic [blue;  $(h, k, l) = (0, 0, 0.5)$ ] and ferromagnetic [orange;  $(h, k, l) = (0, 0, 0.9)$  with structural scattering subtracted] resonant elastic x-ray scattering (REXS) as a function of temperature. AFM scattering onsets sharply at  $T_N$ , in contrast to the gradual onset of ferromagnetism around  $2T_N$ , emphasized in the logarithmic plot in the inset.

order and cannot arise due to fluctuations. Zooming in on the weak feature at  $\sim 2T_N$ , we see peaks in both temperature-modulated birefringence and pMOKE [Fig. 2(d), the inset]. Since the temperature-modulated measurements are sensitive to the temperature derivatives of birefringence and pMOKE, the peaks in the inset correspond to the onsets of the two-order parameters. The simultaneous onsets indicate that the order parameters are likely coupled.

### III. RESONANT X-RAY SCATTERING: FERROMAGNETISM OF $\text{Eu}^{2+}$ IONS

To help identify the origin of rotational symmetry breaking above  $T_N$ , we employed REXS with photon energy tuned to the Eu  $M_5$  edge (1127.5 eV). The amplitude of the (0 0 0.5) diffraction peak, corresponding to A-AFM order, drops sharply at  $T_N = 11.5$  K, ruling out A-AFM order as the source of  $C_3$  breaking above  $T_N$  [Fig. 2(e)]. The ferromagnetic (FM) peak at (0 0 1) is obscured by the structural one; however, a fortunate matrix element suppression of the structural Thomson scattering at (0 0 0.9) provides a window to the FM order (for details see the SI, Sec. IV [20]). In contrast with the AFM onset, the FM order decreases smoothly through  $T_N$

[Fig. 2(f)], mirroring the  $dM_z(T)$  extracted from the pMOKE signal [Fig. 2(d)], and can be traced up to  $\sim 2T_N$  (the inset). We note that our measurements indicate static FM order, in contrast to short-range fluctuations reported in the sibling compound  $\text{EuCd}_2\text{As}_2$  [23].

#### IV. LINEAR MAGNETO-BIREFRINGENCE: TIME REVERSAL SYMMETRY BREAKING AT $\sim 2T_N$

Having confirmed the existence of ferromagnetic order for  $T > T_N$ , we turn to the origin of rotational symmetry breaking above the Néel temperature. In particular, we explore the idea that the rotational symmetry breaking is caused by an in-plane component of magnetization  $M_{\parallel}$ . Although, in principle,  $M_{\parallel}$  can be detected by thermally modulated longitudinal and transverse Kerr effect [22] measured at a finite incidence angle, the large birefringence observed at normal incidence would hinder such experiments. We have, therefore, developed a new method, based on the linear magneto-optic effect [24–30], to isolate rotational symmetry breaking associated with order parameters that break time-reversal symmetry as well. Specifically, we measure the modulation of birefringence that is linear in an applied magnetic field; we refer to this effect as linear magneto-birefringence (LMB), and parametrize it by the LMB tensor,

$$\vec{\delta r} = \begin{pmatrix} \beta & \gamma \\ \gamma & -\beta \end{pmatrix} H_z, \quad (2)$$

where  $\vec{\delta r}$  is the change in reflectance,  $H_z$  is an applied field, and (1, 0) and (0, 1) correspond to the principal axes at  $H_z = 0$ . As a consequence of Onsager's relation, the LMB tensor vanishes in TR invariant systems (see the SI, Sec. V [20] for a derivation), making it a sensitive probe of TR symmetry breaking.

We measure the components of  $\vec{\delta r}$  by detecting the change in reflectivity at the fundamental frequency of an oscillating  $H_z$ , applied by a small coil [31]. After careful calibration of the setup (the SI, Sec. III.C [20]), the change in polarization on reflection that is synchronous with the applied field  $d\phi \sim AH_z \sin[2(\phi + \phi_C)]$  yields the elements of the LMB tensor through the relations,

$$A^2 = \beta^2 + \gamma^2, \quad \phi_C = \phi_0 + \frac{1}{2} \arctan \frac{\gamma}{\beta}, \quad (3)$$

where  $\phi_0$  is the principal axes orientation at  $H_z = 0$ .

Figure 3(a) shows the existence of the LMB in  $\text{EuCd}_2\text{P}_2$  at 16 K. The diamonds and circles compare the change in polarization induced by field and temperature modulation, respectively, and demonstrate a phase shift of  $52^\circ$  between them. The observation of a phase shift that is not equal to either  $0^\circ$  or  $45^\circ$  proves that both  $\beta$  and  $\gamma$  are nonzero [Eq. (3)]. A symmetry analysis of the LMB tensor in  $\text{EuCd}_2\text{P}_2$ , summarized in Fig. 3(b) and discussed in detail in Sec. V of the SI [20], shows that the only component of magnetization which can induce a nonzero  $\gamma$  is  $M_y$ , revealing this component of FM order above  $T_N$ , and identifying it as the origin of birefringence above the AFM transition.

The temperature dependence of the field-modulated amplitude, plotted in Fig. 3(c), shows that the LMB vanishes at  $\sim 2T_N$ , coincident with the disappearance of  $M_z$  [Fig. 2(d)],

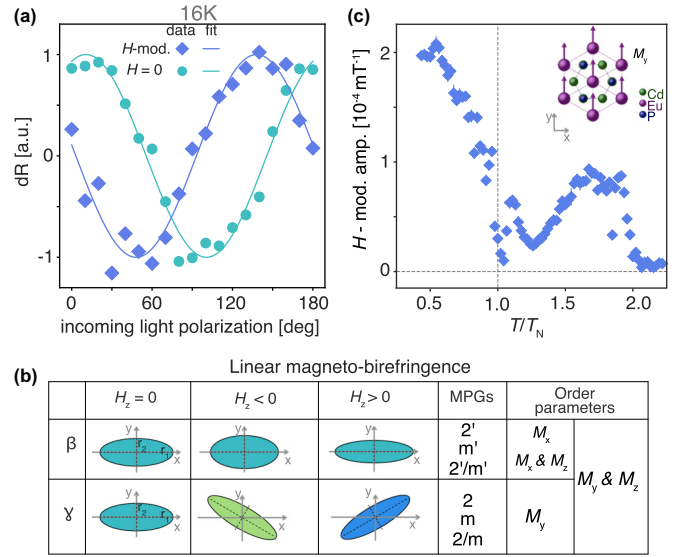


FIG. 3. (a) The phase difference between the  $H_z$ -linear birefringence (diamonds) and the  $H = 0$  birefringence (circles) proves  $\gamma \neq 0$  Eq. (3), and, therefore,  $M_y \neq 0$  [the inset of (c)]. For clarity the curves are normalized by the respective amplitudes, and constant offsets are subtracted. (b) Diagonal ( $\beta$ ) and off-diagonal ( $\gamma$ ) LMB: the orientation and length of the ellipse axes represent the orientation of the optic principal axes and the reflectivity along them, respectively. Magnetic point groups (MPGs) and order parameters compatible with the two effects are listed. (c) The amplitude of the LMB as a function of temperature ( $T_N = 11.5$  K) reveals the onset of TR—and  $C_3$ —broken phase at  $\sim 2T_N$ . Probe beam: 20  $\mu\text{W}$ , 633 nm; field amplitude: 0.2 mT, modulated at 500 Hz.

and the ferromagnetic REXS scattering [Fig. 2(e)]. Although the onset temperature of the LMB signal is reproducible, the details of the LMB amplitude as a function of temperature in the ferromagnetic state depend on the specific domain configuration, which changes on each cool down (see Sec. VI of the SI [20]) as expected of a state which spontaneously breaks time-reversal symmetry.

#### V. INVERTED HYSTERESIS: THE ROLE OF SPIN-CARRIER COUPLING

We have now provided three complementary pieces of evidence for the onset of static ferromagnetism in  $\text{EuCd}_2\text{P}_2$ : pMOKE and LMB, which are directly sensitive to time-reversal symmetry breaking, confirm the presence of  $M_z$  and  $M_y$ , respectively, whereas the elemental specificity and momentum resolution of REXS unambiguously identify Eu atoms in  $\text{EuCd}_2\text{P}_2$  as the source of the ferromagnetism. Motivated by these results, we repeated bulk magnetization measurements, first reported in Ref. [5], on a larger sample to ensure better signal-to-noise ratio, and we were indeed able to observe a small hysteretic moment of 0.01  $\mu_B$  at 3 K, setting a lower bound on the ferromagnetic volume fraction to 0.1% (see Sec. VIII of the SI [20] for the analysis).

We note that  $M_y$  and  $M_z$  correspond to distinct magnetic point groups, so one is not a natural consequence of the other as in “weak ferromagnetism” [32], for example. Their coexistence indicates coupling via a high-order magnetocrystalline

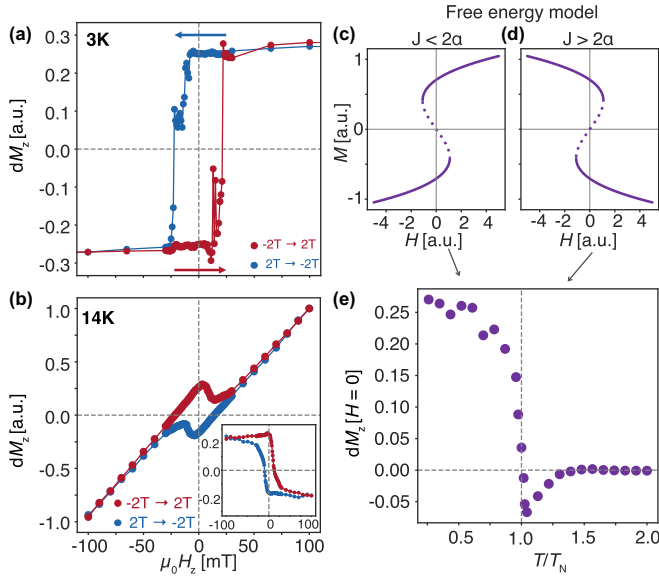


FIG. 4.  $dM_z$  as a function of  $H_z$  for increasing (red) and decreasing (blue) field at (a) 3 K and (b) 14 K, revealing the opposite sense of hysteresis at the two temperatures. Removing the linear background in (b) shows the inverted hysteresis (the inset). (c) and (d) The real solutions of Eq. (6) for (c)  $J < 2\alpha_2$  and (d)  $J > 2\alpha_2$ . The full and dotted lines correspond to local minima and saddle points of the free energy, respectively. (e) The temperature dependence of the magnetization at zero field, defined as half the difference between the  $dM_z(H = 0)$ , measured whereas increasing and decreasing the field.

anisotropy (MCA), which typically arises from a combination of spin-orbit coupling and the crystal field [33]. However, the ground state of  $\text{Eu}^{2+}$  carries no angular momentum [34], so spin-orbit coupling is expected to be negligible, and the anisotropy cannot be understood by considering only Eu spins. Instead, the MCA can stem from the coupling of Eu to the carriers as was previously demonstrated in other magnets containing the  $L = 0$   $\text{Eu}^{2+}$  or  $\text{Gd}^{3+}$  ions [35–37].

Confirmation that ferromagnetism in  $\text{EuCd}_2\text{P}_2$  results from the coupling between Eu spins and conduction electrons comes from measurements of  $dM_z$  as a function of the applied DC magnetic field. Figure 4(a) follows the magnetization through a field sweep at 3 K, showing a hysteresis loop that confirms FM order. The same field sweep conducted at 14 K [Fig. 4(b)] is also hysteretic but looks very different in two respects: the loop proceeds clockwise rather than counterclockwise and is superposed on a linear background. Removing the background (the inset) emphasizes the hysteresis is *inverted*: The saturated magnetization is antiparallel to the applied field direction!

Inverted hysteresis cannot arise from a single class of ferromagnetically coupled spins; instead, at least, two *antiferromagnetically* coupled subsystems are required. A minimum model for the observed behavior is described by the free energy,

$$F = \alpha_2 m^2 + \beta_2 M^2 + \beta_4 M^4 + JmM - H(m + M), \quad (4)$$

where  $m$  and  $M$  are the magnetization of carriers and Eu ions, respectively,  $J$  is the antiferromagnetic coupling between them, and the parameters  $\alpha_n$  and  $\beta_n$  are the quadratic

and quartic terms in the expansion in even powers of the magnetization. With  $H = 0$ ,  $F$  has a minimum at nonzero magnetization,

$$M^2 = \frac{1}{4\beta_4} \left( \frac{J^2}{2\alpha_2} - 2\beta_2 \right), \quad m = -\frac{J}{2\alpha_2} M, \quad (5)$$

for coupling strengths  $J^2 > 4\beta_2\alpha_2$ , showing that  $J$  promotes spontaneous magnetization, even if the uncoupled Eu system would be paramagnetic ( $\beta_2 > 0$ ).

Minimizing the free energy with  $H \neq 0$  yields (the SI, Sec. VII [20]),

$$M^3 - \frac{M}{4\beta_4} \left( \frac{J^2}{2\alpha_2} - 2\beta_2 \right) - \frac{H}{4\beta_4} \left( 1 - \frac{J}{2\alpha_2} \right) = 0. \quad (6)$$

Equation (6) suggests that the effective magnetic field experienced by the Eu spin is opposite in sign to the applied field if  $J$  is larger than  $2\alpha_2$ , yielding the inverted Eu hysteresis. Although the total magnetization,  $M + m$ , is parallel to the applied field, our experiment is dominantly sensitive to Eu magnetization and, therefore, capable of observing its inverted hysteresis. The existence of both normal and inverted Eu hysteresis within this model is demonstrated in Figs. 4(c) and 4(d), which illustrate  $M$  vs  $H$  for  $J < 2\alpha_2$  and  $J > 2\alpha_2$ , respectively. Both regimes exhibit classic bistable behavior with three solutions for  $\partial F/\partial M = \partial F/\partial m = 0$  at low applied field; two stable minima (solid lines) and one saddle point (dashed line). Mirrored trajectories of  $M$  vs  $H_z$  in Figs. 4(c) and 4(d) correspond to normal and inverted hysteresis, respectively.

The temperature dependence of the zero-field magnetization [Fig. 4(e)], defined to be positive for normal hysteresis, shows that the transition from normal to inverted regimes occurs at  $T_N$ . The onset of the antiferromagnetic order, therefore, disrupts the delicate balance required for realization of the inverted hysteresis. Our model suggests that this is caused by a reduction in the effective spin-carrier interaction  $J/\alpha_2$  as expected from the decrease in the spin polarization of the electrons due to their coupling to the AFM order.

## VI. OPTICAL CONDUCTIVITY: ELECTRON LOCALIZATION

These observations of a bulk FM order, and the inverted hysteresis above  $T_N$ , offer compelling evidence for the role of spin-carrier coupling in determining the magnetic properties of  $\text{EuCd}_2\text{P}_2$ . We now turn to the role of this coupling in its remarkable resistivity. To help address this question we augmented our magneto-optical and x-ray probes with measurements of the frequency- and temperature-dependent conductivity  $\sigma_1(\omega, T)$ , obtained by the Kramers-Kronig analysis of broadband reflectivity.

Figure 5(a) shows optical conductivity spectra measured at the resistivity peak (18 K) together with representative spectra measured in the metallic regime at temperatures above (50 K) and below (5 K). The contrast in the spectra between the high and the low conductivity regimes provides a clear picture of the dynamics that underline the giant resistance peak. Although the optical conductivity at 5 and 50 K is remarkably similar,  $\sigma_1(\omega, 18 \text{ K})$  is clearly suppressed at low frequencies. Subtracting the spectrum measured at 18 K from that measured at 5 K reveals a Drude-like peak [Fig. 5(a), inset].

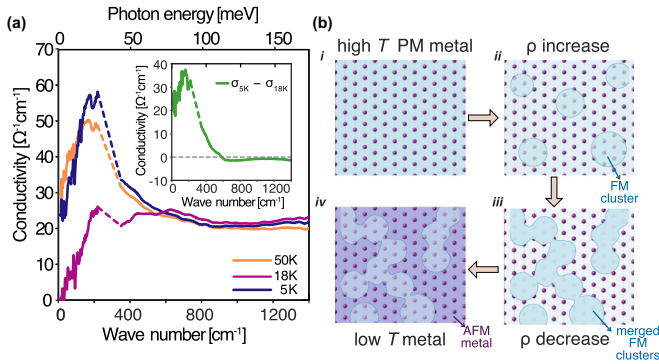


FIG. 5. (a) Optical conductivity at 50, 18, and 5 K, showing electron localization at 18 K. The inset is the difference between the 5- and the 18-K data, showing the conduction electron spectral weight. The dashed lines are interpolations across a region where the measurement is dominated by the spectral weight of an optical phonon. (b) Schematic temperature evolution of the coupled Eu-electron system.

We attribute the metallic conductivity observed in the high- and low-temperature regimes to this component of  $\sigma_1(\omega)$ ; the resistivity peak at 18 K then reflects its vanishing. We note that standard analysis of the optical conductivity and Hall effect (the SI, Sec. IX [20]) yields a carrier concentration  $n_e = 0.6 \times 10^{19} \text{ cm}^{-3}$ , scattering rate  $\Gamma = 9 \times 10^{13} \text{ s}^{-1}$ , and a mass of  $1.5m_e$ , where  $m_e$  is the free-electron mass. The conductivity spectra measured as  $T$  passes through the peak in resistivity confirm that the increase in  $\rho$  originates from a dramatic decrease in  $n_e$  rather than an increase in  $\Gamma$  (Fig. 5(a), and Ref. [38]). Optical conductivity, therefore, offers unambiguous evidence of electron localization.

## VII. CONCLUSION AND OUTLOOK

Although nonmonotonic temperature dependence of resistivity in *nonmagnetic*  $f$ -electron metals is typically attributed to Kondo scattering (see Ref. [34] for a discussion in Eu compounds), a unifying theoretical explanation for resistivity peaks in metallic magnets is lacking [39–42].  $\text{EuCd}_2\text{P}_2$  is an outlier in both the giant amplitude and the location in temperature of the maximum in  $\rho(T)$ . Nonetheless, our combination of optical polarimetry, x-ray, and far-infrared measurements points to spontaneous phase separation, similar to that observed in the *ferromagnetic* metal  $\text{EuB}_6$  [43–45]. In this scenario [Fig. 5(b)] high-temperature metallic behavior is interrupted by phase separation: electrons localize into spin-polarized clusters within which spins align due to the spin-carrier coupling [ $J$  in Eq. (4)]. The localization [Fig. 5(a)] causes the resistivity to increase with decreasing temperature, starting at  $\sim 75$  K. The increase in resistivity is slowed down as percolating conducting paths start to form, eventually causing the resistivity to decrease. The width of the resistivity peak is, therefore, determined by the combination of two processes: ferromagnetic cluster formation and percolation. The percolation picture also helps explain the colossal magnetoresistance reported in Ref. [5]: an externally applied

magnetic field promotes growth of the ferromagnetic clusters and, therefore, percolation, limiting the increase in resistivity in the peak region. The merged clusters develop a net ferromagnetic moment ( $M_y, M_z$ ), detected by our suite of probes (REXS, pMOKE, and LMB). In particular, the spontaneous phase separation is seen in the behavior of the magnetization vs  $H_z$  in this regime [Fig. 4(b)]: paramagnetic Eu spins contribute the linear background, whereas the inverted hysteresis arises in the carrier-mediated ferromagnetic regions.

Our finding that the same process, i.e., the spontaneous formation and percolation of ferromagnetic clusters, is responsible for resistivity in both  $\text{EuCd}_2\text{P}_2$  and  $\text{EuB}_6$ , is surprising. The two compounds exhibit different magnetic order, and drastically different resistivity anomalies: the 100-fold increase in  $\rho$  in the AFM  $\text{EuCd}_2\text{P}_2$  vs the 20% increase in the FM  $\text{EuB}_6$ . We suggest that the low carrier density and the frustration resulting from near degeneracy of ferro- and antiferromagnetic states in  $\text{EuCd}_2\text{P}_2$  are the key ingredients yielding the enhanced effect. These ingredients are then principles that can guide the design of other systems in which transport displays hypersensitivity to external control parameters, such as temperature and electromagnetic fields. Furthermore, our paper motivates future experiments to directly visualize the ferromagnetic clusters, as well as the development of a unified theoretical description of resistivity in a wide range of systems with strong carrier-spin interactions and offers ways to experimentally constrain such models.

## ACKNOWLEDGMENTS

We thank E. Dagotto, A. Mackenzie, C. Liu, M. Vila Tusell, T. Scaffidi, and E. Altman for useful discussions. Optical measurements were performed at the Lawrence Berkeley Laboratory as part of the Quantum Materials Program, Director, Office of Science, Office of Basic Energy Sciences, Materials Sciences and Engineering Division of the U.S. Department of Energy under Contract No. DE-AC02-05CH11231. V.S. was supported by the Miller Institute for Basic Research in Science, UC Berkeley. J.O. and Y.S. received support from the Gordon and Betty Moore Foundation’s EPiQS Initiative through Grant No. GBMF4537 to J.O. at UC Berkeley. F.T. and S.B. acknowledge funding from the Schiller Institute Grant for Exploratory Collaborative Scholarship (SIGECS). E.D. acknowledges support from the National Science Foundation Graduate Research Fellowship under Grant No. DGE-2146752. S.B-C thanks the MINECO of Spain through the project PGC2018-101334-A-C22. A.F. acknowledges support from the Research Corporation for Science Advancement via the Cottrell Scholar Award (27551) and the CIFAR Azrieli Global Scholars program. Work at Brookhaven National Laboratory was supported by the Office of Science, U.S. Department of Energy under Contract No. DE-SC0012704. This material was based upon work supported by the National Science Foundation under Grant No. DMR-2145080, and the National Science Foundation Graduate Research Fellowship under Grant No. DGE-2038238.

- [1] M. E. Fisher and J. S. Langer, Resistive Anomalies at Magnetic Critical Points, *Phys. Rev. Lett.* **20**, 665 (1968).
- [2] J.-Z. Ma, S. M. Nie, C. J. Yi, J. Jandke, T. Shang, M. Y. Yao, M. Naamneh, L. Q. Yan, Y. Sun, A. Chikina, V. N. Strocov, M. Medarde, M. Song, Y.-M. Xiong, G. Xu, W. Wulfhchel, J. Mesot, M. Reticcioli, C. Franchini, C. Mudry, M. Müller, Y. G. Shi, T. Qian, H. Ding, and M. Shi, Spin fluctuation induced Weyl semimetal state in the paramagnetic phase of  $\text{EuCd}_2\text{As}_2$ , *Sci. Adv.* **5**, eaaw4718 (2019).
- [3] Y. Xu, L. Das, J. Z. Ma, C. J. Yi, S. M. Nie, Y. G. Shi, A. Tiwari, S. S. Tsirkin, T. Neupert, M. Medarde, M. Shi, J. Chang, and T. Shang, Unconventional Transverse Transport above and below the Magnetic Transition Temperature in Weyl Semimetal  $\text{EuCd}_2\text{As}_2$ , *Phys. Rev. Lett.* **126**, 076602 (2021).
- [4] M. C. Rahn, J.-R. Soh, S. Francoual, L. S. I. Veiga, J. Stremper, J. Mardegan, D. Y. Yan, Y. F. Guo, Y. G. Shi, and A. T. Boothroyd, Coupling of magnetic order and charge transport in the candidate Dirac semimetal  $\text{EuCd}_2\text{As}_2$ , *Phys. Rev. B* **97**, 214422 (2018).
- [5] Z.-C. Wang, J. D. Rogers, X. Yao, R. Nichols, K. Atay, B. Xu, J. Franklin, I. Sochnikov, P. J. Ryan, D. Haskel, and F. Tafti, Colossal magnetoresistance without mixed valence in a layered phosphide crystal, *Adv. Mater.* **33**, 2005755 (2021).
- [6] H. Su, B. Gong, W. Shi, H. Yang, H. Wang, W. Xia, Z. Yu, P.-J. Guo, J. Wang, L. Ding, L. Xu, X. Li, X. Wang, Z. Zou, N. Yu, Z. Zhu, Y. Chen, Z. Liu, K. Liu, G. Li, and Y. Guo, Magnetic exchange induced Weyl state in a semimetal  $\text{EuCd}_2\text{Sb}_2$ , *APL Mater.* **8**, 011109 (2020).
- [7] Y. Zhang, K. Deng, X. Zhang, M. Wang, Y. Wang, C. Liu, J.-W. Mei, S. Kumar, E. F. Schwier, K. Shimada, C. Chen, and B. Shen, In-plane antiferromagnetic moments and magnetic polaron in the axion topological insulator candidate  $\text{EuIn}_2\text{As}_2$ , *Phys. Rev. B* **101**, 205126 (2020).
- [8] Y. Xu, Z. Song, Z. Wang, H. Weng, and X. Dai, Higher-Order Topology of the Axion Insulator  $\text{EuIn}_2\text{As}_2$ , *Phys. Rev. Lett.* **122**, 256402 (2019).
- [9] G. Hua, S. Nie, Z. Song, R. Yu, G. Xu, and K. Yao, Dirac semimetal in type-IV magnetic space groups, *Phys. Rev. B* **98**, 201116(R) (2018).
- [10] J.-R. Soh, F. de Juan, M. G. Vergniory, N. B. M. Schröter, M. C. Rahn, D. Y. Yan, J. Jiang, M. Bristow, P. Reiss, J. N. Blandy, Y. F. Guo, Y. G. Shi, T. K. Kim, A. McCollam, S. H. Simon, Y. Chen, A. I. Coldea, and A. T. Boothroyd, Ideal Weyl semimetal induced by magnetic exchange, *Phys. Rev. B* **100**, 201102(R) (2019).
- [11] L.-L. Wang, N. H. Jo, B. Kuthanazhi, Y. Wu, R. J. McQueeney, A. Kaminski, and P. C. Canfield, Single pair of Weyl fermions in the half-metallic semimetal  $\text{EuCd}_2\text{As}_2$ , *Phys. Rev. B* **99**, 245147 (2019).
- [12] J.-R. Soh, C. Donnerer, K. M. Hughes, E. Schierle, E. Weschke, D. Prabhakaran, and A. T. Boothroyd, Magnetic and electronic structure of the layered rare-earth pnictide  $\text{EuCd}_2\text{Sb}_2$ , *Phys. Rev. B* **98**, 064419 (2018).
- [13] X. Gui, I. Pletikoscic, H. Cao, H.-J. Tien, X. Xu, R. Zhong, G. Wang, T.-R. Chang, S. Jia, T. Valla, W. Xie, and R. J. Cava, A new magnetic topological quantum material candidate by design, *ACS Cent. Sci.* **5**, 900 (2019).
- [14] S. X. M. Riberolles, T. V. Trevisan, B. Kuthanazhi, T. W. Heitmann, F. Ye, D. C. Johnston, S. L. Bud'ko, D. H. Ryan, P. C. Canfield, A. Kreyssig, A. Vishwanath, R. J. McQueeney, L.-L. Wang, P. P. Orth, and B. G. Ueland, Magnetic crystalline-symmetry-protected axion electrodynamics and field-tunable unpinned Dirac cones in  $\text{EuIn}_2\text{As}_2$ , *Nat. Commun.* **12**, 999 (2021).
- [15] K. M. Taddei, L. Yin, L. D. Sanjeeva, Y. Li, J. Xing, C. dela Cruz, D. Phelan, A. S. Sefat, and D. S. Parker, Single pair of Weyl nodes in the spin-canted structure of  $\text{EuCd}_2\text{As}_2$ , *Phys. Rev. B* **105**, L140401 (2022).
- [16] J. Krishna, T. Nautiyal, and T. Maitra, First-principles study of electronic structure, transport, and optical properties of  $\text{EuCd}_2\text{As}_2$ , *Phys. Rev. B* **98**, 125110 (2018).
- [17] N. H. Jo, B. Kuthanazhi, Y. Wu, E. Timmons, T.-H. Kim, L. Zhou, L.-L. Wang, B. G. Ueland, A. Palasyuk, D. H. Ryan, R. J. McQueeney, K. Lee, B. Schruck, A. A. Burkov, R. Prozorov, S. L. Bud'ko, A. Kaminski, and P. C. Canfield, Manipulating magnetism in the topological semimetal  $\text{EuCd}_2\text{As}_2$ , *Phys. Rev. B* **101**, 140402(R) (2020).
- [18] N. H. Jo, Y. Wu, T. V. Trevisan, L.-L. Wang, K. Lee, B. Kuthanazhi, B. Schruck, S. L. Bud'ko, P. C. Canfield, P. P. Orth, and A. Kaminski, Visualizing band selective enhancement of quasiparticle lifetime in a metallic ferromagnet, *Nat. Commun.* **12**, 7169 (2021).
- [19] E. Gati, S. L. Bud'ko, L.-L. Wang, A. Valadkhani, R. Gupta, B. Kuthanazhi, L. Xiang, J. M. Wilde, A. Sapkota, Z. Guguchia, R. Khasanov, R. Valentí, and P. C. Canfield, Pressure-induced ferromagnetism in the topological semimetal  $\text{EuCd}_2\text{As}_2$ , *Phys. Rev. B* **104**, 155124 (2021).
- [20] See Supplemental Material at <https://link.aps.org/supplemental/10.1103/PhysRevB.107.144404> for additional information.
- [21] A. Little, C. Lee, C. John, S. Doyle, E. Maniv, N. L. Nair, W. Chen, D. Rees, J. W. F. Venderbos, R. M. Fernandes, J. G. Analytis, and J. Orenstein, Three-state nematicity in the triangular lattice antiferromagnet  $\text{Fe}_{1/3}\text{NbS}_2$ , *Nature Mater.* **19**, 1062 (2020).
- [22] Y. Sun, C. Lee, H.-Y. Yang, D. H. Torchinsky, F. Tafti, and J. Orenstein, Mapping domain-wall topology in the magnetic Weyl semimetal  $\text{CeAlSi}$ , *Phys. Rev. B* **104**, 235119 (2021).
- [23] J.-R. Soh, E. Schierle, D. Y. Yan, H. Su, D. Prabhakaran, E. Weschke, Y. F. Guo, Y. G. Shi, and A. T. Boothroyd, Resonant x-ray scattering study of diffuse magnetic scattering from the topological semimetals  $\text{EuCd}_2\text{As}_2$  and  $\text{EuCd}_2\text{Sb}_2$ , *Phys. Rev. B* **102**, 014408 (2020).
- [24] N. F. Kharchenko, V. V. Eremenko, and O. P. Tutakina, Light birefringence bilinear in the ferromagnetic and antiferromagnetic vectors in cobalt carbonate, *Pisma Zh. Exp. Teor. Fiz* **27**, 466 (1978).
- [25] N. F. Kharchenko, V. V. Eremenko, and L. I. Belyi, Lowering of the optical class of an antiferromagnetic crystal, induced by a longitudinal magnetic field, *Pisma Zh. Exp. Teor. Fiz* **28**, 351 (1978).
- [26] N. Kharchenko and S. Gnatchenko, Linear magneto-optic effect and visual observation of anti-ferromagnetic domains in orthorhombic  $\text{DyFeO}_3$  crystal, *Fiz. Nyzk. Temp.* **7**, 475 (1981).
- [27] V. V. Eremenko and N. F. Kharchenko, Magneto-optics of anti-ferromagnets, *Phys. Rep.* **155**, 379 (1987).
- [28] V. V. Eremenko, N. F. Kharchenko, L. I. Belyi, and O. P. Tutakina, Birefringence of the antiferromagnetic crystals linear in a magnetic field, *J. Magn. Magn. Mater.* **15-18**, 791 (1980).

- [29] V. V. Eremenko, Y. G. Litvinenko, N. K. Kharchenko, and V. M. Naumenko, Magneto-optical methods for investigating the structure of antiferromagnetically ordered crystals, in *Magneto-Optics and Spectroscopy of Antiferromagnets*, edited by V. V. Eremenko, Y. G. Litvinenko, N. K. Kharchenko, and V. M. Naumenko (Springer, New York, 1992), pp. 67–110.
- [30] N. F. Kharchenko, The linear magneto-optic effect as a manifestation of a higher order magnetoelectric effect, *Ferroelectrics* **162**, 173 (1994).
- [31] C. Lee, P. Vir, K. Manna, C. Shekhar, J. E. Moore, M. A. Kastner, C. Felser, and J. Orenstein, Observation of a phase transition within the domain walls of ferromagnetic  $\text{Co}_3\text{Sn}_2\text{S}_2$ , *Nat. Commun.* **13**, 3000 (2022).
- [32] I. Dzyaloshinsky, A thermodynamic theory of “weak” ferromagnetism of antiferromagnetics, *J. Phys. Chem. Solids* **4**, 241 (1958).
- [33] R. Skomski, P. Manchanda, and A. Kashyap, Anisotropy and crystal field, in *Handbook of Magnetism and Magnetic Materials*, edited by M. Coey and S. Parkin (Springer, Cham, 2021), pp. 1–83.
- [34] Y. Ōnuki, M. Hedo, and F. Honda, Unique electronic states of Eu-based compounds, *J. Phys. Soc. Jpn.* **89**, 102001 (2020).
- [35] M. Colarieti-Tosti, S. I. Simak, R. Ahuja, L. Nordström, O. Eriksson, D. Åberg, S. Edvardsson, and M. S. S. Brooks, Origin of Magnetic Anisotropy of Gd Metal, *Phys. Rev. Lett.* **91**, 157201 (2003).
- [36] S. Abdelouahed and M. Alouani, Magnetic anisotropy in Gd, GdN, and  $\text{GdFe}_2$  tuned by the energy of gadolinium 4f states, *Phys. Rev. B* **79**, 054406 (2009).
- [37] M. Blanco-Rey, R. Castrillo-Bodero, K. Ali, P. Gargiani, F. Bertran, P. M. Sheverdyaeva, J. E. Ortega, L. Fernandez, and F. Schiller, Effect of the valence state on the band magnetocrystalline anisotropy in two-dimensional rare-earth/noble-metal compounds, *Phys. Rev. Res.* **4**, 013237 (2022).
- [38] C. C. Homes, Z.-C. Wang, K. Fruhling, and F. Tafti, Optical properties and carrier localization in the layered phosphide  $\text{EuCd}_2\text{P}_2$ , *Phys. Rev. B* **107**, 045106 (2023).
- [39] C. Timm, M. E. Raikh, and F. von Oppen, Disorder-Induced Resistive Anomaly Near Ferromagnetic Phase Transitions, *Phys. Rev. Lett.* **94**, 036602 (2005).
- [40] Z. Wang, K. Barros, G.-W. Chern, D. L. Maslov, and C. D. Batista, Resistivity Minimum in Highly Frustrated Itinerant Magnets, *Phys. Rev. Lett.* **117**, 206601 (2016).
- [41] B. Flebus, Magnetoresistance driven by the magnetic Berezinskii-Kosterlitz-Thouless transition, *Phys. Rev. B* **104**, L020408 (2021).
- [42] E. Heinrich, T. Posske, and B. Flebus, Topological magnetic phase transition in Eu-based A-type antiferromagnets, *Phys. Rev. B* **106**, 214402 (2022).
- [43] M. Pohlit, S. Rößler, Y. Ohno, H. Ohno, S. von Molnár, Z. Fisk, J. Müller, and S. Wirth, Evidence for Ferromagnetic Clusters in the  $\text{EuB}_6$ , *Phys. Rev. Lett.* **120**, 257201 (2018).
- [44] P. Das, A. Amyan, J. Brandenburg, J. Müller, P. Xiong, S. von Molnár, and Z. Fisk, Magnetically driven electronic phase separation in the semimetallic ferromagnet  $\text{EuB}_6$ , *Phys. Rev. B* **86**, 184425 (2012).
- [45] M. L. Brooks, T. Lancaster, S. J. Blundell, W. Hayes, F. L. Pratt, and Z. Fisk, Magnetic phase separation in  $\text{EuB}_6$  detected by muon spin rotation, *Phys. Rev. B* **70**, 020401(R) (2004).